

Spin/momentum properties of the paraxial optical beams

Peng Shi, Heng Li, Luping Du*, Xiaocong Yuan*

Institute of Micro/Nano Optoelectronics, Shenzhen University, 518060, China

*Authors to whom correspondence should be addressed: lpdu@szu.edu.cn, and xcyuan@szu.edu.cn

Abstract: Spin angular momentum, an elementary dynamical property of classical electromagnetic fields, plays an important role in spin–orbit and light–matter interactions, especially in near-field optics. The research on optical spins has led to the discovery of phenomena such as optical spin–momentum locking and photonic topological quasiparticles, as well as applications in high-precision detection and nanometrology. Here, we investigate spin–momentum relations in paraxial optical systems and show that the optical spin angular momentum contains transverse and longitudinal spin components simultaneously. The transverse spin originates from inhomogeneities of field and governed by the vorticity of the kinetic momentum density, whereas the longitudinal spin parallel to the local canonical momentum is proportional to the polarization ellipticity of light. Moreover, the skyrmion-like spin textures arise from the optical transverse spin can be observed in paraxial beams, and their topologies are maintained free from the influence of the Gouy phase during propagation. Interestingly, the optical singularities, including both phase and polarization singularities, can also affect the spin–momentum properties significantly. Our findings describe the intrinsic spin–momentum properties in paraxial optical systems and apply in the analysis of the properties of spin–momentum in optical focusing, imaging, and scattering systems.

Keywords. *Spin angular momentum of light, spin-momentum locking, optical skyrmions, paraxial light, structured light*

I. Introduction

Spin angular momentum (SAM) is a fundamental dynamical property of elementary particles and classical wave fields^{1–14} and plays a critical role in understanding spin–orbit^{15–29} and wave–matter^{1,2,30–32} interactions and predicting the behavior of interacting systems. For a classical electromagnetic (EM) field, the SAM associated with circular or elliptical polarization can be orientated in an arbitrary direction^{15,16,33,34}. From this general perspective, for plane-wave solutions of Maxwell’s equations, the SAM component oriented along the propagating direction (defined by the wavevector or canonical momentum) is considered as the longitudinal spin³³ (L-spin), whereas the SAM component oriented perpendicular to the wavevector is the transverse spin³⁴ (T-spin). To date, T-spins have been intensively investigated in various EM systems, including confined optical systems such as evanescent waves^{35–40}, guided modes^{41–45}, and free-space optical systems such as the Gaussian focused fields^{46–50}, interference fields⁵¹, nondiffracting fields⁵², and unpolarized fields^{53–56}. Remarkably, in confined optical systems, the T-spins of evanescent and guided modes feature a well-known property referred to as spin–momentum locking^{36,41,42,57,58} and their spin–orbit couplings raise a large class of remarkable phenomena, such as unidirectional guided wave^{59–67} and photonic topological quasiparticles^{68–78}, and offer potential applications in angular-momentum-based optical manipulation^{37,49,50,79,80}, imaging^{81–93}, detection^{94–96}, metrology^{97,98}, and on-chip quantum technologies⁹⁹.

Previously, in free space, only the spin properties of special optical beams were investigated^{46–52}. However, for an arbitrary structured light which carries the inhomogeneities of intensity, phase, polarization and singularities^{100–105}, a unified methodology is lacking in describing the dynamical evolving of momentum and angular momentum, especially regarding paraxial focusing, imaging, and scattering systems. Moreover, although optical beams in the free space can form skyrmionic beams^{106–118}, the Gouy phase governs the continuous evolution of polarization structures in the propagating beam, whereas SAM is a good candidate in describing the topological invariants of propagating optical beams. Therefore, understanding the spin–momentum properties of paraxial optical fields is meaningful in providing a guide for spin-state manipulation.

Here, we investigate the spin–momentum properties of paraxial optical systems and present a unified methodology to perform the decomposition of the optical spin into T-spin and L-spin for various types of paraxial optical beams. The results reveal that there are optical T-spins that govern optical spin–momentum locking and L-spins determined by the polarization ellipticities (helicities) that are parallel to the canonical momentum in paraxial optical beams. Remarkably, from the spin–momentum locking derived from optical T-spin, skyrmion-like spin textures can form in paraxial optical beams and their topologies are maintained during propagation, free from the influence of the Gouy phase. We furthermore investigate the influence of optical singularities on the spin–momentum properties in paraxial optical systems and discover an extraordinary SAM component. The direction of its vector, which is perpendicular to that of canonical momentum, is not determined by the vorticity of the kinetic momentum but by the polarization topological charge of the vector vortex beam. This SAM component is characterized by \mathbb{Z}_4 topological invariants and should be considered as a L-spin. Our findings are general for high-order structured light beams constructed through the linear superpositions of paraxial optical modes and can help in the understanding of the dynamical properties of light and broadens the study of topological quasiparticles in paraxial systems.

II Theory

General theoretical results

For monochromatic, time-harmonic EM waves in the paraxial approximation with complex electric field strength \mathbf{E} and magnetic field strength \mathbf{H} having angular frequency dependence ω , we demonstrate that the kinetic momentum $\mathbf{p} = \text{Re}\{\mathbf{E}^* \times \mathbf{H}\}/2c^2$, with c the velocity of light in vacuo, and the SAM $\mathbf{S} = \text{Im}\{\varepsilon(\mathbf{E}^* \times \mathbf{E}) + \mu(\mathbf{H}^* \times \mathbf{H})\}/4\omega$, with ε and μ the permittivity and permeability of the vacuum and superscript * signifying complex conjugation^{119–123}, have an inherent relationship given by

$$\mathbf{S}_T = \frac{1}{2k^2} \nabla \times \mathbf{p} \quad \text{and} \quad \mathbf{S}_L = \mathbf{S} - \mathbf{S}_T. \quad (1)$$

Here, $k = \omega/c$ denotes the wave number, \mathbf{S}_T and \mathbf{S}_L denote the optical T-spin and L-spin, respectively. These equations show that, in the paraxial optical systems, the T-spin stems from the field inhomogeneities and given by the vorticity of the kinetic momentum density. The transversality of the optical T-spin is confirmed from the identity $\nabla \cdot (\nabla \times \mathbf{A}) = 0$. However, it does not mean that the curl of the kinetic momentum is always perpendicular to the kinetic momentum. By decomposing the structured light into a superposition of plane waves, the perpendicularity of the momentum vector and the optical T-spin vector is satisfied for each plane wave basis, as for example the evanescent plane wave^{35,36}. Remarkably, the T-spin is capable of producing spin–momentum locking^{36,41,42,57}, i.e., if the kinetic momentum is reversed, the T-spin is inverted correspondingly. In addition, the T-spin is a classical physical quantity, and the kinetic momentum describing the group velocity of photons is considered as

the current of light^{119,121}. Thus, spin–momentum locking from the T-spin, which may also be considered as spin–current locking, originates from the intrinsic spin–orbit property inherent in Maxwell’s equations and is different from the quantum spin Hall effect in condensed matter physics¹²⁴.

In contrast, the L-spin is extracted by subtracting the T-spin from the total SAM. In the following, we shall demonstrate that this difference, which is related to the three-dimensional (3D) polarization ellipticities along the local wavevector^{15–17} and the Berry curvature of paraxial optical fields¹⁵, is definitely the L-spin. Here, we primarily focus our attention on the spin–momentum properties of the paraxial modes, the solutions of the Helmholtz equation, in both Cartesian and cylindrical coordinates, and high-order structured light beams constructed from linear superpositions of these modes^{125–130}.

Spin-momentum property of Hermite-Gaussian beams

We first consider a Hermite-Gaussian (HG) beam, the solution to the Helmholtz equation in the paraxial approximation in Cartesian coordinates (x, y, z) with unit vector ($\hat{\mathbf{x}}, \hat{\mathbf{y}}, \hat{\mathbf{z}}$), propagating along the z axis. The electric and magnetic field components can be expressed as

$$\mathbf{E}_{\text{HG}} = \left[+\eta_x u_{\text{HG}} \hat{\mathbf{x}}, +\eta_y u_{\text{HG}} \hat{\mathbf{y}}, +\frac{1}{ik} \left(\eta_x \frac{\partial}{\partial x} + \eta_y \frac{\partial}{\partial y} \right) u_{\text{HG}} \hat{\mathbf{z}} \right]^T e^{-ikz} \quad (2)$$

and

$$\mathbf{H}_{\text{HG}} = \frac{k}{\omega\mu} \left[+\eta_y u_{\text{HG}} \hat{\mathbf{x}}, -\eta_x u_{\text{HG}} \hat{\mathbf{y}}, +\frac{1}{ik} \left(\eta_y \frac{\partial}{\partial x} - \eta_x \frac{\partial}{\partial y} \right) u_{\text{HG}} \hat{\mathbf{z}} \right]^T e^{-ikz}, \quad (3)$$

where η_x and η_y are arbitrary complex constants describing the relative strength, $\text{Im}\{\eta_x^* \eta_y\}$ specifies the polarization ellipticity (helicity) of the paraxial HG beam, and the superscript T indicates the transpose of the matrix. The electric field \mathbf{E}_{HG} and magnetic field \mathbf{H}_{HG} also satisfy Gauss’s law ($\nabla \cdot \mathbf{E}_{\text{HG}} = 0$ and $\nabla \cdot \mathbf{H}_{\text{HG}} = 0$) in the paraxial approximation ($\frac{\partial^2 u_{\text{HG}}}{\partial z^2} \ll k \frac{\partial u_{\text{HG}}}{\partial z} \ll k^2 u_{\text{HG}}$). The complex amplitude u_{HG} is given by

$$u_{\text{HG},mn} = \frac{w_0}{w(z)} H_m \left[\frac{\sqrt{2}x}{w(z)} \right] H_n \left[\frac{\sqrt{2}y}{w(z)} \right] \exp \left(-\frac{x^2 + y^2}{w^2(z)} - i \frac{k(x^2 + y^2)}{2R(z)} \right) \exp \left(-i(1+m+n)\tan^{-1}\left(\frac{z}{z_R}\right) \right). \quad (4)$$

Here, $H_m(x)$ is the Hermite polynomial with non-negative integer index m , $z_R = \pi w_0^2 / \lambda$ the Rayleigh range, $w(z) = w_0 \sqrt{1 - z^2/z_R^2}$ the beam width of the propagating wave, w_0 the beam radius at the beam waist, $R(z)$ the radius of curvature of the wavefronts, λ the wavelength, and the last factor $\exp(-i(1+m+n)\tan^{-1}(z/z_R))$ is the Gouy phase¹⁰⁷. From Equation 2, 3, and 4, one finds that the paraxial HG beam displays both intensity and phase inhomogeneities, whereas the polarization is homogeneous in the transverse propagating plane (xy -plane).

Employing Equation 2 and 3, the kinetic momentum of paraxial HG beam is

$$\mathbf{p} = \frac{\varepsilon k}{2\omega} \text{Re} \left(\begin{array}{l} \left(\frac{1}{ik} \left[+(\eta_x^* \eta_x + \eta_y^* \eta_y) u_{\text{HG}}^* \frac{\partial u_{\text{HG}}}{\partial x} + \eta_x^* \eta_y \frac{\partial u_{\text{HG}}^* u_{\text{HG}}}{\partial y} \right] \hat{\mathbf{x}} \right) \\ \left(\frac{1}{ik} \left[+(\eta_x^* \eta_x + \eta_y^* \eta_y) u_{\text{HG}}^* \frac{\partial u_{\text{HG}}}{\partial y} - \eta_x^* \eta_y \frac{\partial u_{\text{HG}}^* u_{\text{HG}}}{\partial x} \right] \hat{\mathbf{y}} \right) \\ \left(\frac{1}{ik} \left[-ik(\eta_x \eta_x^* + \eta_y \eta_y^*) u_{\text{HG}}^* u_{\text{HG}} - 0 \right] \hat{\mathbf{z}} \right) \end{array} \right). \quad (5)$$

From the spin–orbit decomposition theory of the kinetic momentum for classical EM fields^{41,42,119,121}, the kinetic momentum of an optical field can be decomposed into canonical and spin momentum components ($\mathbf{p} = \mathbf{p}_o + \mathbf{p}_s$). One recognizes the first term in Equation 5 as the canonical momentum ($\mathbf{p}_o \propto \langle \psi | i\nabla | \psi \rangle$ with ψ the 6-vector photonic wave function^{131,132}), and the z -component of the canonical momentum as being proportional to the energy density ($(\eta_x^* \eta_x + \eta_y^* \eta_y) u_{HG}^* u_{HG}$). In contrast, the second term in Equation 5 is the Belinfante spin momentum $\mathbf{p}_s = \nabla \times \mathbf{S}/2$ ^{119,121}, in which the SAM is proportional to the polarization ellipticity $\text{Im}\{\eta_x^* \eta_y\} u_{HG}^* u_{HG}$ ³³. Generally, for structured light beams, the Belinfante spin momentum is nonzero, and thus the kinetic momentum is not parallel to the canonical momentum, which determines the local wavevector \mathbf{k} through relation $\mathbf{p}_o = \hbar \mathbf{k}$.

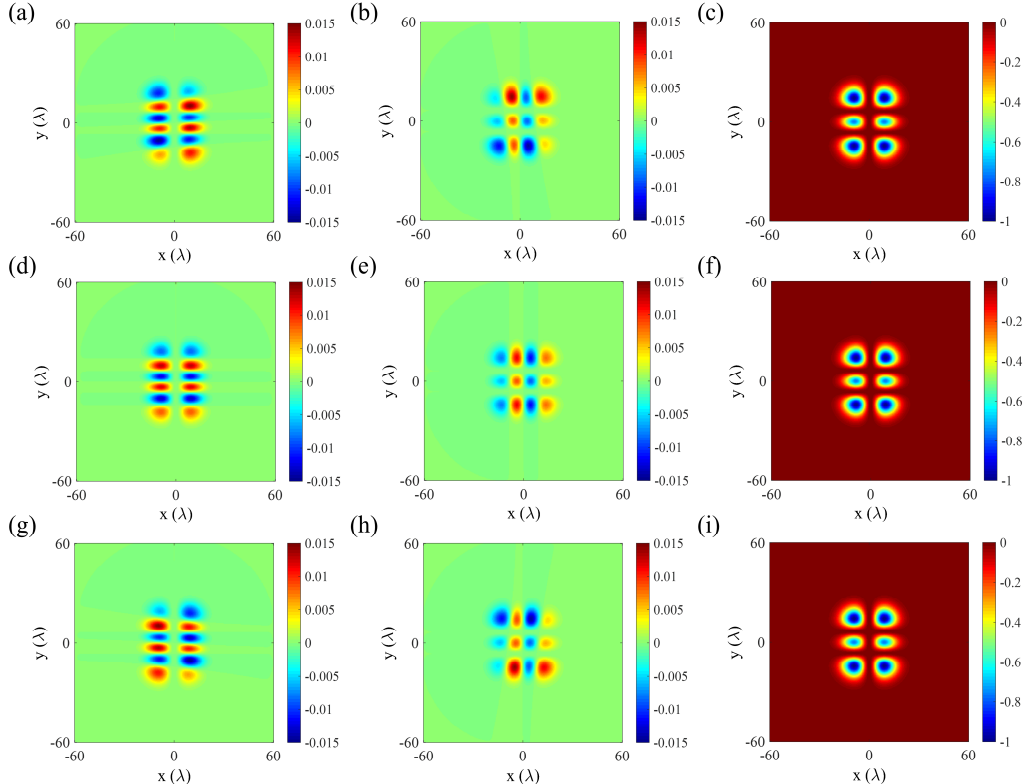


Figure 1. Momentum properties of paraxial HG₁₂ beams in the pre-focal, focal and post-focal planes: (a) x -component p_x , (b) y -component p_y , and (c) z -component p_z of the kinetic momentum at plane $z = -100\lambda$. By analyzing their vector structure, the horizontal kinetic momentum components contain multiple vortex structures. The z -component kinetic momentum is always nonzero, hence the photons of this HG beam precess during propagation. (d–f) as for (a–c), but at plane $z = 0.001\lambda$; (g–i) same as (a–c), but at plane $z = +100\lambda$. Here, $\eta_x = 1$, $\eta_y = 2i$, $w_0 = 8 \mu\text{m}$, $\lambda = 0.6328 \mu\text{m}$.

To understand the momentum properties of paraxial HG beams, we plot the three components of the kinetic momentum densities for the HG₁₂ mode in the pre-focal plane, focal plane, and post-focal plane in Figure 1. From Figure 1a-b, d-e, and g-h, the horizontal kinetic momenta differ slightly through convergence in the pre-focal plane and divergence in the post-focal plane compared with those in the focal plane. By analyzing the vector properties of these horizontal kinetic momentum densities, one can find that they contain multiple vortex structures (Figure 3a). Moreover, from Figure 1c, f and i, one finds that the z -component kinetic momenta in these planes are parallel. Thus, the photons of this paraxial HG mode precess around the z -axis and these spiral trajectories of the photons give rise to the geometric phase^{133–135}. Note that the Gouy phase in Equation 4 does not affect the properties of the kinetic momenta

when the beam passes through the focal plane, and thus the vortex structures of the kinetic momenta remain unchanged during propagation.

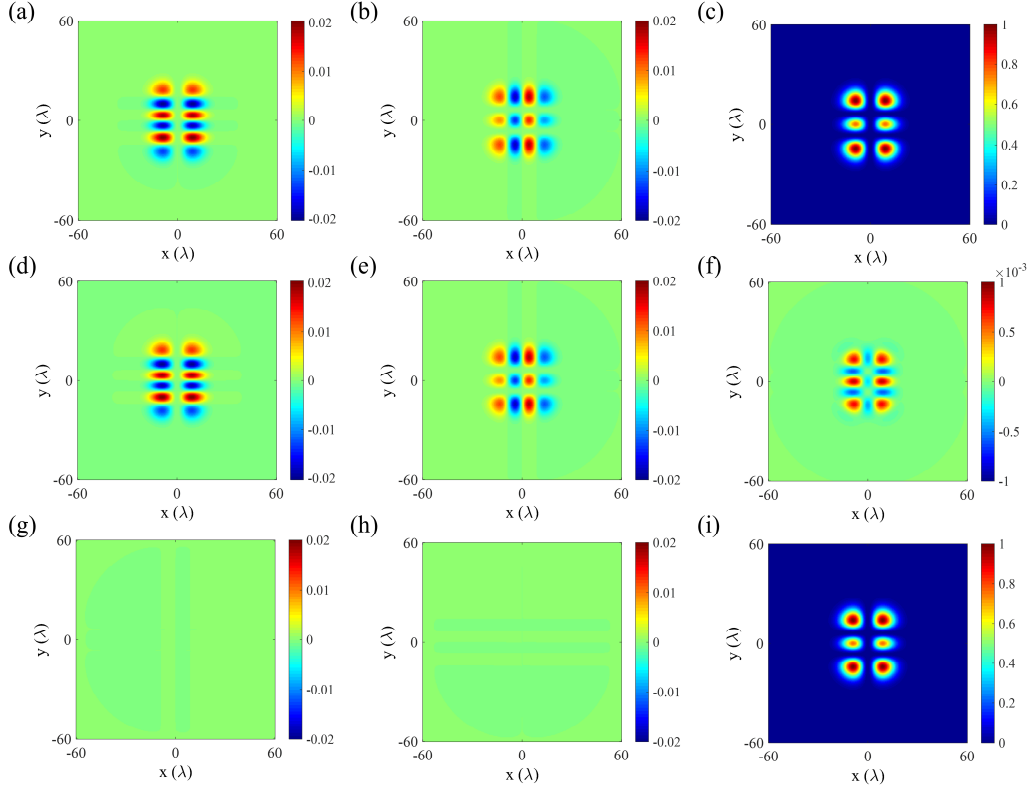


Figure 2. Spin properties of paraxial HG₁₂ beams in the focal plane. The total spin is three dimensional with: (a) x -component S_x , (b) y -component S_y , and (c), z -component S_z . The total spin decomposes into a T-spin that contributes to spin-momentum locking and a L-spin determined by the polarization ellipticities. The (d) x - and (e) y -component T-spins originate from the inhomogeneity of the kinetic momentum density and the (f) z -component T-spin relates to the Berry curvature. For the L-spin, the x - and y -components, (g) and (h) respectively, are considered as projections of the z -component (i) onto the horizontal axes. In the plane $z = 0.001\lambda$, both components are too small and can be ignored. The beam parameter settings are same as given in Figure 1.

To exhibit the spin property of the paraxial HG beam, the total SAM and the decomposed T-spin and L-spin given in Equation 1 were calculated,

$$\mathbf{S} = \frac{\epsilon}{4\omega} \text{Im} \left\{ \begin{array}{l} \left[\frac{1}{ik} \left[+(\eta_x^* \eta_x + \eta_y^* \eta_y) \frac{\partial u_{\text{HG}}^* u_{\text{HG}}}{\partial y} - (\eta_x^* \eta_y - \eta_y^* \eta_x) \left(u_{\text{HG}}^* \frac{\partial u_{\text{HG}}}{\partial x} - u_{\text{HG}} \frac{\partial u_{\text{HG}}^*}{\partial x} \right) \right] \hat{\mathbf{x}} \right. \\ \left. - \left[-(\eta_x^* \eta_x + \eta_y^* \eta_y) \frac{\partial u_{\text{HG}}^* u_{\text{HG}}}{\partial x} - (\eta_x^* \eta_y - \eta_y^* \eta_x) \left(u_{\text{HG}}^* \frac{\partial u_{\text{HG}}}{\partial y} - u_{\text{HG}} \frac{\partial u_{\text{HG}}^*}{\partial y} \right) \right] \hat{\mathbf{y}} \right\}, \\ 2[\eta_x^* \eta_y - \eta_y^* \eta_x] u_{\text{HG}}^* u_{\text{HG}} \hat{\mathbf{z}} \end{array} \right\}, \quad (6)$$

$$\mathbf{S}_T = \frac{1}{2k^2} \nabla \times \mathbf{p} = \frac{\varepsilon}{4\omega} \text{Im} \left\{ \begin{array}{l} \frac{1}{ik} \left[+(\eta_x^* \eta_x + \eta_y^* \eta_y) \frac{\partial u_{\text{HG}}^* u_{\text{HG}}}{\partial y} \right] \hat{\mathbf{x}} \\ \frac{1}{ik} \left[-(\eta_x^* \eta_x + \eta_y^* \eta_y) \frac{\partial u_{\text{HG}}^* u_{\text{HG}}}{\partial x} \right] \hat{\mathbf{y}} \\ \frac{1}{k^2} \left[(\eta_x^* \eta_x + \eta_y^* \eta_y) (\nabla u_{\text{HG}}^* \times \nabla u_{\text{HG}})_z - \frac{1}{2} (\eta_x^* \eta_y - \eta_y^* \eta_x) \nabla_{\perp}^2 (u_{\text{HG}}^* u_{\text{HG}}) \right] \hat{\mathbf{z}} \end{array} \right\}, \quad (7)$$

and

$$\mathbf{S}_L = \frac{\varepsilon}{4\omega} \text{Im} \left\{ \begin{array}{l} \frac{1}{ik} \left[-(\eta_x^* \eta_y - \eta_y^* \eta_x) \left(u_{\text{HG}}^* \frac{\partial u_{\text{HG}}}{\partial x} - u_{\text{HG}} \frac{\partial u_{\text{HG}}^*}{\partial x} \right) \right] \hat{\mathbf{x}} \\ \frac{1}{ik} \left[-(\eta_x^* \eta_y - \eta_y^* \eta_x) \left(u_{\text{HG}}^* \frac{\partial u_{\text{HG}}}{\partial y} - u_{\text{HG}} \frac{\partial u_{\text{HG}}^*}{\partial y} \right) \right] \hat{\mathbf{y}} \\ \left[\begin{array}{l} 2(\eta_x^* \eta_y - \eta_y^* \eta_x) u_{\text{HG}}^* u_{\text{HG}} \\ -\frac{1}{k^2} (\eta_x^* \eta_x + \eta_y^* \eta_y) (\nabla u_{\text{HG}}^* \times \nabla u_{\text{HG}})_z + \frac{1}{2k^2} (\eta_x^* \eta_y - \eta_y^* \eta_x) \nabla_{\perp}^2 (u_{\text{HG}}^* u_{\text{HG}}) \end{array} \right] \hat{\mathbf{z}} \end{array} \right\}. \quad (8)$$

The total SAM given in Equation 6 are plotted in Figure 2a-c. The first terms of the horizontal SAMs are T-spins (Equation 7), which originate from the inhomogeneities of the EM fields and are proportional to the transverse gradients of the kinetic momenta in the paraxial approximation^{17,41,42}; see Figure 2d-f. The other terms comprise the L-spin, which is determined by the polarization ellipticity of the EM field; see Figure 2g-i. The horizontal components of L-spin in Equation 8 can be understood further by considering the complex amplitude u_{HG} as an approximate superposition of plane waves ($\exp(i(k_x x + k_y y))$)¹²⁵, and hence satisfy $\partial u_{\text{HG}}/\partial x = ik_x u_{\text{HG}}$, $\partial u_{\text{HG}}/\partial y = ik_y u_{\text{HG}}$ with k_x/k and k_y/k representing the horizontal directional vector components. Thus, these horizontal SAM components can be regarded as projections of the L-spin onto the horizontal axes when the EM wave is either converging or diverging. In this way, the horizontal SAM components are nearly zero at the focal plane; see Figure 2g-h.

Moreover, from the analysis above, the photons of paraxial HG modes possess spiral trajectories, leading to strong spin-orbit coupling, as evident in the z -component T-spin (Equation 9). Therein, the first term ($\text{Im}\{\nabla u_{\text{HG}}^* \times \nabla u_{\text{HG}}\} \propto \nabla \times \mathbf{p}_o$) has a similar form to the Berry curvature of the optical potential^{173,136}, which is related to the evolution of the geometric phase in a paraxial optical system. The last term in Equation 7 originates from the vorticity of spin momentum \mathbf{p}_s , i.e., $\nabla \times \mathbf{p}_s = -\nabla^2 \mathbf{S}/2 \approx -\hat{\mathbf{z}} \text{Im}\{\eta_x^* \eta_y - \eta_y^* \eta_x\} \nabla_{\perp}^2 (u_{\text{HG}}^* u_{\text{HG}})$ and $\mathbf{S} \approx \hat{\mathbf{z}} 2 \text{Im}\{\eta_x^* \eta_y - \eta_y^* \eta_x\} u_{\text{HG}}^* u_{\text{HG}}$. Here, the transverse Laplace operator is $\nabla_{\perp}^2 = \partial^2/\partial x^2 + \partial^2/\partial y^2$. The physical meaning of this quantity can be further understood in a more general context. Employing the spin-orbit decomposition to calculate the vorticity of the kinetic momentum directly, one obtains⁴¹

$$\begin{aligned} \mathbf{S}_t &= \frac{1}{2k^2} \nabla \times \mathbf{p} = \frac{1}{2k^2} \nabla \times (\mathbf{p}_o + \mathbf{p}_s) = \frac{1}{2k^2} \left(-\frac{1}{\omega} \langle \nabla \psi | \times i | \nabla \psi \rangle - \frac{1}{2} \nabla^2 \mathbf{S} \right) \\ &= \frac{\mathbf{S}}{2} - \frac{1}{8\omega^2} \text{Re} \left\{ \begin{array}{l} -(\nabla \otimes \mathbf{E}^*) \cdot \mathbf{H} - (\nabla \otimes \mathbf{E})^T \cdot \mathbf{H}^* \\ + (\nabla \otimes \mathbf{H}^*) \cdot \mathbf{E} + (\nabla \otimes \mathbf{H})^T \cdot \mathbf{E}^* \end{array} \right\}, \end{aligned} \quad (9)$$

where

$$\mathbf{r}_1 \otimes \mathbf{r}_2 = \begin{pmatrix} x_1x_2 & y_1x_2 & z_1x_2 \\ x_1y_2 & y_1y_2 & z_1y_2 \\ x_1z_2 & y_1z_2 & z_1z_2 \end{pmatrix}. \quad (10)$$

The T-spin given by the vorticity of kinetic momentum has a similar structure to the quantum 2-form¹³⁷ that generates the Berry phase associated with a circuit. Thus, the z -component of T-spin (Equation 7) can be regarded as the Berry curvature of the optical potential that originates from the spiral trajectories of photons. If polarization ellipticity is absent ($\eta_x = 0$ or $\eta_y = 0$ or the η_x and η_y are in-phase), the photons do not undergo spiral trajectories and thus the z -component T-spin is nearly zero, i.e., no Berry phase is generated in this instance. These Berry curvature-related terms are also included in the expression for L-spin (Equation 8) because they describe the evolution of the polarization ellipticities during propagation. Note that for paraxial optical systems the conditions imposed are $\partial^2/\partial x^2 \ll k \partial/\partial x \ll k^2$ and $\partial^2/\partial y^2 \ll k \partial/\partial y \ll k^2$ (as considered in Figure 2) and the integrals of the horizontal component of the L-spin and the Berry curvature-related term on the transverse plane are zero; one then concludes that the SAMs are conserved in the paraxial approximation, in agreement with references¹³⁸⁻¹⁴¹. In summary, Equation 8, which represents the projection of the polarization ellipticity onto the 3D axes and includes the Berry curvature, is definitely the L-spin component.

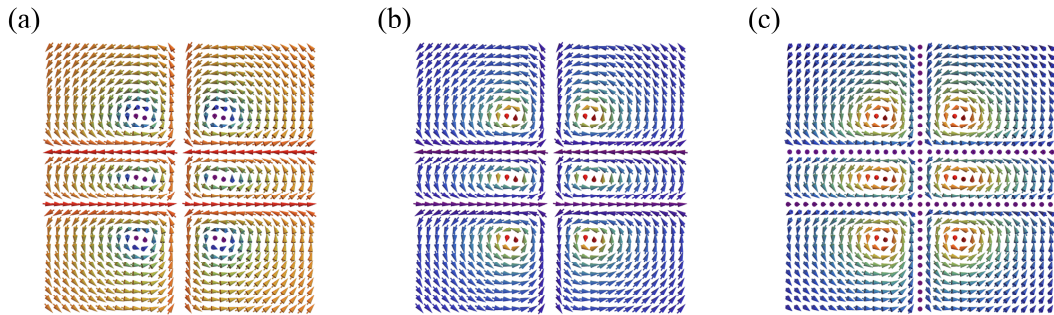


Figure 3. Momentum and spin textures of the paraxial HG₁₂ beam: (a) The vector diagram of kinetic momentum at the focal plane. The horizontal components contain multiple vortex structures, and thus the photons precess around the z -axis. (b) The normalized spin vector of the total spin. For each texture, the spin vector varies from the center “up” state to the boundary “horizontal” state, and thus the skyrmion number of each spin texture is $-1/2$ (half-skyrmion). (c) The normalized spin vector of the T-spin. The T-spin vectors vary from the center “up” state to the boundary “down” state and rotate in helical spirals, which is a manifestation of a Bloch-type skyrmion. The skyrmion number of each skyrmion-like spin texture is equal to -1 . Skyrmion-like spin textures are formed in each transverse plane through spin-momentum locking of the T-spin and their topologies are maintained during propagation, free from the influence of the Gouy phase. Here, the topological number (skyrmion number) is calculated from $N = \iint_{\sigma} \mathbf{m} \cdot (\partial \mathbf{m}/\partial x \times \partial \mathbf{m}/\partial y)/4\pi$ ⁶⁸, where $\mathbf{m} = \mathbf{S}/|\mathbf{S}|$ is the normalized spin vector.

In the confined optical field, a vortex structure of the kinetic momentum may result in a skyrmion-like spin texture^{41,42,68}. Here, if there is a nonvanishing polarization ellipticity ($\text{Im}\{\eta_x^* \eta_y - \eta_y^* \eta_x\} \neq 0$), a similar vortex structure for the horizontal kinetic momentum is observed (Figure 3a). The vortex structure of the horizontal kinetic momentum causes the formation a skyrmion-like spin texture with T-spin through spin-momentum locking of the T-spin (Figure 3b, c). In contrast to the confined field case in which the spin vector of spin texture rotates in cycloidal spirals (Néel-type skyrmion), the spin texture

of the paraxial HG beam possesses a Bloch-type configuration (Figure 3c), for which the spin vector rotates in helical spirals. Moreover, the skyrmion-like spin texture manifest spin–momentum locking and the kinetic momentum is maintained during propagation. Thus, the topology of the skyrmion-like spin texture is also unchanged during propagation and is unaffected by the evolution of the Gouy phase, in contrast to that of a paraxial skyrmionic beam¹⁰⁷. Note that if there is a local disturbance (such as a nanoparticle) causing a kinetic momentum deflection, the topology of the skyrmion-like spin texture breaks down. The skyrmion number of each skyrmion-like spin texture is -1 when the polarization ellipticity $\text{Im}\{\eta_x^*\eta_y - \eta_y^*\eta_x\} > 0$.

Spin-momentum property of Laguerre-Gaussian beams carrying phase singularities.

Next, we consider a paraxial Laguerre-Gaussian (LG) beam¹⁴² propagating along the z axis in the cylindrical coordinates (ρ, φ, z) with unit vector $(\hat{\mathbf{p}}, \hat{\mathbf{q}}, \hat{\mathbf{z}})$. The electric and magnetic field components become

$$\mathbf{E}_{\text{LG}} = \left[\eta_x u_{\text{LG}} \hat{\mathbf{x}}, \eta_y u_{\text{LG}} \hat{\mathbf{y}}, +\frac{1}{ik} \left[(\eta_x \cos \varphi + \eta_y \sin \varphi) \frac{\partial u_{\text{LG}}}{\partial \rho} + (-\eta_x \sin \varphi + \eta_y \cos \varphi) \frac{iu_{\text{LG}}}{\rho} \right] \hat{\mathbf{z}} \right] e^{-ikz}, \quad (11)$$

and

$$\mathbf{H}_{\text{LG}} = \frac{k}{\omega\mu} \left[\eta_y u_{\text{LG}} \hat{\mathbf{x}}, -\eta_x u_{\text{LG}} \hat{\mathbf{y}}, \frac{1}{ik} \left[(-\eta_x \sin \varphi + \eta_y \cos \varphi) \frac{\partial u_{\text{LG}}}{\partial \rho} - (\eta_x \cos \varphi + \eta_y \sin \varphi) \frac{iu_{\text{LG}}}{\rho} \right] \hat{\mathbf{z}} \right] e^{-ikz}. \quad (12)$$

Here, η_x and η_y are arbitrary complex constants describing the relative strength and polarization ellipticity, respectively. We use these expressions to ensure the polarization state is homogeneous in the transverse plane. The electric field \mathbf{E}_{LG} and magnetic field \mathbf{H}_{LG} satisfy Gauss's law ($\nabla \cdot \mathbf{E}_{\text{LG}} = 0$ and $\nabla \cdot \mathbf{H}_{\text{LG}} = 0$) in the paraxial approximation. The complex amplitude u_{LG} is given by

$$u_{\text{LG},pl} = \frac{w_0}{w(z)} \left[\frac{\sqrt{2}\rho}{w(z)} \right]^l L_p^l \left[\frac{2\rho^2}{w^2(z)} \right] \exp \left(-\frac{\rho^2}{w^2(z)} - i \frac{k\rho^2}{2R(z)} \right) \exp(il\varphi) \exp \left(-i(1+2p+|l|) \tan^{-1} \left(\frac{z}{z_R} \right) \right). \quad (13)$$

Here, $L_p^l(x)$ denotes the generalized Laguerre polynomial, l the topological charge of vortex phase, and $\exp(-i(1+2p+|l|)\tan^{-1}(z/z_R))$ is the Gouy phase. From Equation 11 and 12, one obtains the kinetic momentum of the paraxial LG beam,

$$\mathbf{P} = \frac{1}{2} \frac{k}{\omega\mu} \text{Re} \left\{ \begin{aligned} & \frac{1}{ik} \left[+(\eta_\rho^* \eta_\rho + \eta_\varphi^* \eta_\varphi) u_{\text{LG}}^* \frac{\partial u_{\text{LG}}}{\partial \rho} + \eta_\rho^* \eta_\varphi \frac{1}{\rho} \frac{\partial u_{\text{LG}}^* u_{\text{LG}}}{\partial \varphi} \right] \hat{\mathbf{p}} \\ & \frac{1}{ik} \left[+(\eta_\rho^* \eta_\rho + \eta_\varphi^* \eta_\varphi) u_{\text{LG}}^* \frac{1}{\rho} \frac{\partial u_{\text{LG}}}{\partial \varphi} - \eta_\rho^* \eta_\varphi \frac{\partial u_{\text{LG}}^* u_{\text{LG}}}{\partial \rho} \right] \hat{\mathbf{q}} \\ & \frac{1}{ik} \left[-ik(\eta_\rho^* \eta_\rho + \eta_\varphi^* \eta_\varphi) u_{\text{LG}}^* u_{\text{LG}} - 0 \right] \hat{\mathbf{z}} \end{aligned} \right\}, \quad (14)$$

which has a similar form to that of Equation 5. Here, we use substitutions $\eta_\rho = \eta_x \cos \varphi + \eta_y \sin \varphi$ and $\eta_\varphi = -\eta_x \sin \varphi + \eta_y \cos \varphi$. Thus, through energy conservation, the polarization ellipticities are $\eta_\rho^* \eta_\varphi - \eta_\varphi^* \eta_\rho = \eta_x^* \eta_y - \eta_y^* \eta_x$ and $\eta_\rho^* \eta_\rho + \eta_\varphi^* \eta_\varphi = \eta_x^* \eta_x + \eta_y^* \eta_y$. In this instance, η_ρ and η_φ are φ -dependent with $\partial \eta_\rho / \partial \varphi = \eta_\varphi$ and $\partial \eta_\varphi / \partial \varphi = -\eta_\rho$. The kinetic momentum of the paraxial LG₂₁ beam is found from Figure 4a, b. The first and second terms of Equation 14 are the canonical momentum and the Belinfante spin momentum, respectively, and $\partial u_{\text{LG}}^* u_{\text{LG}} / \partial \varphi = 0$. The paraxial LG beam carries phase singularities, which are associated with the orbital angular momenta (OAMs) of light¹⁴². In general, the

photons of paraxial LG beam possess spiral trajectories, which derive from both the SAM and OAM of light.

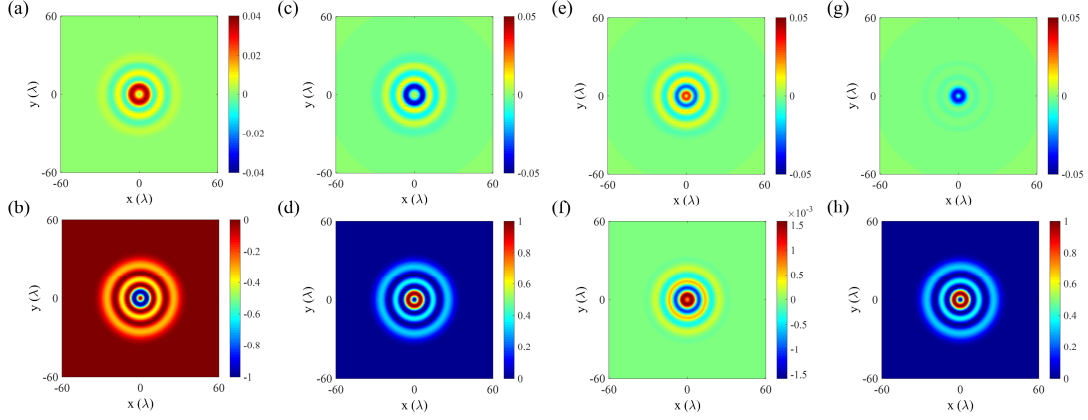


Figure 4. Spin–momentum properties of paraxial LG_{21} beams in the focal plane $z = 0.001\lambda$: (a) azimuthal p_φ and (b) z -component p_z kinetic momenta result in spiral trajectories of the photons (the radial SAM vanishes in the focal plane); (c) azimuthal S_φ and (d) z -component S_z spin angular momenta decompose into T-spin and L-spin; (e) azimuthal T-spin stems from the radial gradient of z -component kinetic momentum density whereas (f) z -component T-spin is related to the Berry curvature; (g) azimuthal L-spins are considered projections of (h), the z -component L-spin onto the azimuthal direction. Here, $\eta_x = 1$, $\eta_y = 2i$, $w_0 = 8 \mu\text{m}$, $\lambda = 0.6328 \mu\text{m}$.

To exhibit the spin property of the paraxial LG beam, the total SAM and the decomposed T-spin and L-spin are expressed in the form

$$\mathbf{S} = \frac{\varepsilon}{4\omega} \text{Im} \left(\begin{array}{l} \frac{1}{ik} \left[0 - (\eta_\rho^* \eta_\varphi - \eta_\varphi^* \eta_\rho) \left(u_{\text{LG}}^* \frac{\partial u_{\text{LG}}}{\partial \rho} - u_{\text{LG}}^* \frac{\partial u_{\text{LG}}^*}{\partial \rho} \right) \right] \hat{\mathbf{p}} \\ \frac{1}{ik} \left[-(\eta_\rho^* \eta_\rho + \eta_\varphi^* \eta_\varphi) \frac{\partial u_{\text{LG}}^* u_{\text{LG}}}{\partial \rho} - (\eta_\rho^* \eta_\varphi - \eta_\varphi^* \eta_\rho) \left(u_{\text{LG}}^* \frac{1}{\rho} \frac{\partial u_{\text{LG}}}{\partial \varphi} - u_{\text{LG}} \frac{1}{\rho} \frac{\partial u_{\text{LG}}^*}{\partial \varphi} \right) \right] \hat{\Phi} \\ 2 [\eta_\rho^* \eta_\varphi - \eta_\varphi^* \eta_\rho] u_{\text{LG}}^* u_{\text{LG}} \hat{\mathbf{z}} \end{array} \right), \quad (15)$$

$$\mathbf{S}_T = \frac{1}{2k^2} \nabla \times \mathbf{p} = \frac{\varepsilon}{4\omega} \text{Im} \left(\begin{array}{l} 0 \hat{\mathbf{p}} \\ \frac{1}{ik} \left[-(\eta_\rho^* \eta_\rho + \eta_\varphi^* \eta_\varphi) \frac{\partial u_{\text{LG}}^* u_{\text{LG}}}{\partial \rho} \right] \hat{\Phi} \\ \frac{1}{k^2} \left[(\eta_\rho^* \eta_\rho + \eta_\varphi^* \eta_\varphi) (\nabla u_{\text{LG}}^* \times \nabla u_{\text{LG}})_z - \frac{1}{2} (\eta_\rho^* \eta_\varphi - \eta_\varphi^* \eta_\rho) \nabla_\perp^2 (u_{\text{LG}}^* u_{\text{LG}}) \right] \hat{\mathbf{z}} \end{array} \right), \quad (16)$$

and

$$\mathbf{S}_L = \frac{\varepsilon}{4\omega} \text{Im} \left\{ \begin{aligned} & \frac{1}{ik} \left[-(\eta_\rho^* \eta_\varphi - \eta_\varphi^* \eta_\rho) \left(u_{\text{LG}}^* \frac{\partial u_{\text{LG}}}{\partial \rho} - u_{\text{LG}} \frac{\partial u_{\text{LG}}^*}{\partial \rho} \right) \right] \hat{\mathbf{p}} \\ & \frac{1}{ik} \left[-(\eta_\rho^* \eta_\varphi - \eta_\varphi^* \eta_\rho) \left(u_{\text{LG}}^* \frac{1}{\rho} \frac{\partial u_{\text{LG}}}{\partial \varphi} - u_{\text{LG}} \frac{1}{\rho} \frac{\partial u_{\text{LG}}^*}{\partial \varphi} \right) \right] \hat{\mathbf{p}} \\ & \left[+2(\eta_\rho^* \eta_\varphi - \eta_\varphi^* \eta_\rho) u_{\text{LG}}^* u_{\text{LG}} \right. \\ & \left. - \frac{1}{k^2} \left[(\eta_\rho^* \eta_\rho + \eta_\varphi^* \eta_\varphi) (\nabla u_{\text{LG}}^* \times \nabla u_{\text{LG}}) + \frac{1}{2} (\eta_\rho^* \eta_\varphi - \eta_\varphi^* \eta_\rho) \nabla_\perp^2 (u_{\text{LG}}^* u_{\text{LG}}) \right] \right] \hat{\mathbf{z}} \end{aligned} \right\}. \quad (17)$$

The total spin components, Equation 15, are shown in Figure 4c, d. The first terms of the horizontal SAMs, which are proportional to the transverse gradients of the kinetic momenta, are T-spins, Equation 16, which are plotted in Figure 4e, f, whereas the other terms comprise the L-spin, Equation 17, which are plotted in Figure 4g, h. The horizontal L-spin components are regarded as projections of the total L-spin onto the horizontal axis as evident from Equation 8.

As mentioned above, for the paraxial LG modes, if the total angular momentum is nonzero, the photons exhibit spiral trajectories¹⁴². Interestingly, either the SAM or the OAM associated spiral trajectories generates a Berry phase. Thus, the z -component of the T-spin in Equation 16 and the last two terms in Equation 17 are related to the Berry curvature of the optical potential associated with the spiral trajectories of photons. If polarization ellipticity is absent ($\eta_x = 0$ or $\eta_y = 0$ or η_x and η_y are in-phase), the photons of the paraxial LG modes also possess spiral trajectories and a nonvanishing Berry curvature ($\text{Im}\{\nabla u_{\text{LG}}^* \times \nabla u_{\text{LG}}\} \neq 0$) also exists. This is the primary distinction between the paraxial HG beam without optical singularities and the paraxial LG beam carrying phase singularities.

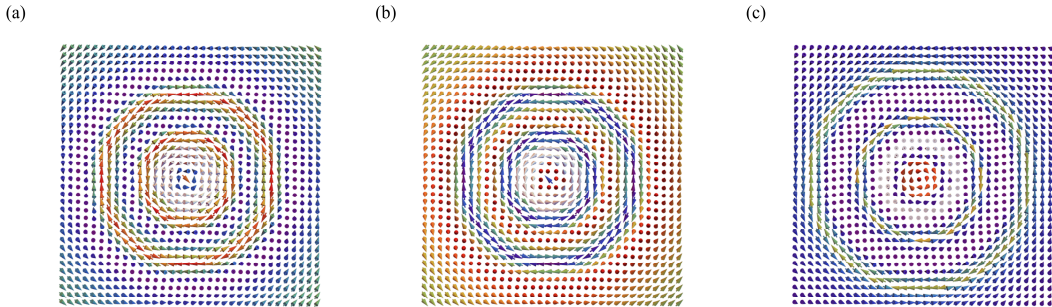


Figure 5. Momentum and spin vectors of the paraxial LG_{21} beam: (a) The vector diagram of kinetic momentum at the focal plane. The horizontal components contain multiple vortex structures (along the radial direction), and thus the photons precess around the z -axis. (b) The normalized spin vector of the total spin. The spin vector varies from the center “up” state to boundary “horizontal” state in the radial direction, and thus the skyrmion number of each spin texture is $-1/2$ (half-skyrmion). (c) The normalized spin vector of the T-spin. For the center spin texture, the T-spin vectors vary from the center “up” state to boundary “down” state and rotate in helical spirals. The skyrmion number of this skyrmion-like spin texture is equal to -1 . As the radius increases, the z -component T-spin is too small and the spin texture is unidentifiable.

In addition, for the paraxial system, the conditions $\partial^2/\partial\rho^2 \ll k \partial/\partial\rho \ll k^2$ and $1/k\rho \ll 1$ apply, the integrals of the horizontal component of L-spin and the Berry curvature-related term on the transverse plane are zero, and the SAMs are conserved in the paraxial approximation. Overall, Equation 17, which describes the 3D polarization ellipticity and Berry curvature, definitively defines the L-spin.

From Equation 14-17 and the above analysis, one finds that the introduction of phase singularities produces an additional contribution to spin-momentum locking, specifically, an OAM-associated Berry curvature in the T-spin. This OAM-associated Berry curvature was also reported in references^{126,127}. In addition, the kinetic momentum of paraxial LG mode contains the vortex structure (Figure 5a), and hence the skyrmionlike spin texture constructed by T-spin appears at the center (Figure 5b, c).

Spin-momentum property of Bessel-Gaussian beams carrying polarization singularities.

Finally, we consider a paraxial Bessel-Gaussian (BG) mode¹⁴³ carrying polarization singularities propagating along the z axis in cylindrical coordinates (ρ, φ, z) with unit vectors $(\hat{\mathbf{p}}, \hat{\mathbf{\Phi}}, \hat{\mathbf{z}})$. The electric and magnetic field components become

$$\mathbf{E}_{\text{BG}} = \left[\cos \Phi u_{\text{BG}} \hat{\mathbf{p}}, \sin \Phi u_{\text{BG}} \hat{\mathbf{\Phi}}, \frac{1}{ik} \left[\frac{1}{\rho} \frac{\partial \rho u_{\text{BG}}}{\partial \rho} + \frac{(n-1)u_{\text{BG}}}{\rho} \right] \cos \Phi \hat{\mathbf{z}} \right]^T e^{-ikz}, \quad (18)$$

and

$$\mathbf{H}_{\text{BG}} = \frac{k}{\omega \mu} \left[\sin \Phi u_{\text{BG}} \hat{\mathbf{p}}, -\cos \Phi u_{\text{BG}} \hat{\mathbf{\Phi}}, \frac{1}{ik} \left[\frac{1}{\rho} \frac{\partial \rho u_{\text{BG}}}{\partial \rho} + \frac{(n-1)u_{\text{BG}}}{\rho} \right] \sin \Phi \hat{\mathbf{z}} \right] e^{-ikz}. \quad (19)$$

Here, we use the substitution $\Phi = [(n-1)\varphi + \varphi_0]$ with φ_0 the initial angle of the polarization state. When $n = 0$, the electric/magnetic field distributions prescribe a paraxial Gaussian beam carrying a homogeneous polarization. For $n \neq 0$, the polarization state is inhomogeneous in the transverse propagating plane and depends on the azimuthal coordinate φ . There is a polarization singularity at the center of the BG beam. The electric field \mathbf{E}_{BG} and magnetic field \mathbf{H}_{BG} also satisfy Gauss' law ($\nabla \cdot \mathbf{E}_{\text{BG}} = 0$ and $\nabla \cdot \mathbf{H}_{\text{BG}} = 0$) in the paraxial approximation. The complex amplitude u_{BG} is given by¹⁴³

$$u_{\text{BG}} = \frac{1}{1 + iz/z_R} \exp \left(-\frac{\rho^2/w_0^2}{1 + iz/z_R} \right) \exp \left[-\frac{i\beta^2 z/(2k)}{1 + iz/z_R} \right] J_n \left(\frac{\beta \rho}{1 + iz/z_R} \right), \quad (20)$$

where β denotes a constant that determines the beam profile (β is positive for this study), and J_n the n -order Bessel function of the first kind. From the expressions for the electric and magnetic fields of these BG modes, one obtains a kinetic momentum of

$$\mathbf{p} = \frac{1}{2} \frac{k}{\omega \mu} \text{Re} \left[\frac{1}{ik} \left[+u_{\text{BG}}^* \frac{\partial u_{\text{BG}}}{\partial \rho} \right] \hat{\mathbf{p}}, 0 \hat{\mathbf{\Phi}}, \frac{1}{ik} \left[-ik u_{\text{BG}}^* u_{\text{BG}} \right] \hat{\mathbf{z}} \right]. \quad (21)$$

In the case, there is only canonical momentum, and Belinfante spin momentum is zero approximately (Figure 6a, e). Moreover, the photons do not possess spiral trajectories ($p_\varphi = 0$) and no Berry phase is generated. The total SAM and its T-spin and L-spin components are

$$\mathbf{S} = \frac{\epsilon}{4\omega} \text{Im} \left[0 \hat{\mathbf{p}}, \frac{1}{ik} \left[-\frac{\partial u_{\text{BG}}^* u_{\text{BG}}}{\partial \rho} - 2n \frac{u_{\text{BG}}^* u_{\text{BG}}}{\rho} \right] \hat{\mathbf{\Phi}}, 0 \hat{\mathbf{z}} \right]^T, \quad (22)$$

$$\mathbf{S}_T = \frac{1}{2k^2} \nabla \times \mathbf{p} = \frac{\epsilon}{4\omega} \text{Im} \left[0 \hat{\mathbf{p}}, \frac{1}{ik} \left[-\frac{\partial u_{\text{BG}}^* u_{\text{BG}}}{\partial \rho} \right] \hat{\mathbf{\Phi}}, 0 \hat{\mathbf{z}} \right]^T, \quad (23)$$

and

$$\mathbf{S}_L = \frac{\epsilon}{4\omega} \text{Im} \left[0 \hat{\mathbf{p}}, \frac{1}{ik} \left[-2 \frac{n u_{\text{BG}}^* u_{\text{BG}}}{\rho} \right] \hat{\mathbf{\Phi}}, 0 \hat{\mathbf{z}} \right]^T. \quad (24)$$

In Equation 22, one finds that the total SAM (Figure 6b, f) contains two terms: the azimuthal SAMs, which are proportional to the transverse gradients of kinetic momenta, are T-spins (Figure 6c, g) as given in Equation 23, whereas the other terms are determined by the polarization topological charge. When the polarization topological charge $n = 0$, the polarization state is homogeneous; the result is consistent with that of Equation 8, i.e., no L-spin exists. However, if $n \neq 0$, the directional vector of this SAM component is determined by the inherent property of the mode, namely, the polarization topological charge (Figure 6d, h). Thus, this SAM component in Equation 24 can be regarded as an L-spin, although it is localized in the transverse plane of the kinetic momentum. This extraordinary L-spin, which does not generate spin-momentum locking but is a \mathbb{Z}_4 topological invariant, is interesting and was discovered quite recently^{44,57}. Obviously, no skyrmion-like spin textures arise because the z -component SAM vanishes. In summary, the introduction of polarization singularities in the paraxial beam creates an extraordinary L-spin but no skyrmion-like spin textures.

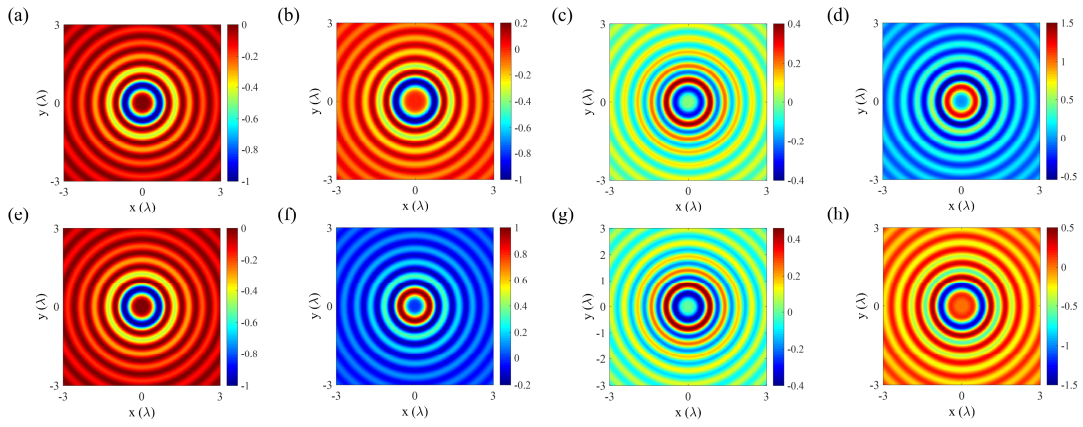


Figure 6. Spin-momentum properties of paraxial BG beams in the focal plane $z = 0$: (a) z -component kinetic momentum p_z , (b) azimuthal optical spin S_ϕ , (c) optical T-spin, (d) optical L-spin for the +3-order paraxial BG beams, (e) z -component kinetic momentum p_z , (f) azimuthal optical spin S_ϕ , (g) optical T-spin, and (h) optical L-spin for the -3-order paraxial BG beam. The other components are zero. From (a) and (e), the kinetic momenta are the same, and thus the T-spin are also the same; see (c) and (g). However, the L-spin is inverted when the polarization topological charge switches between +3 and -3. This spin, which is independent of the vorticity of kinetic momentum but depends on the polarization singularity, is the L-spin (and is a \mathbb{Z}_4 topological invariant). Here, $w_0 = 8 \mu\text{m}$, $\lambda = 0.6328 \mu\text{m}$.

III Conclusion

To summarize, we presented a unified methodology to describe the spin-momentum properties in the paraxial optical systems. The theory uncovers the underlying physical difference between T-spin and L-spin. Moreover, the decomposition of T-spin is consistent with the Helmholtz decomposition theory¹⁴⁴ and can be generalized to other classical wave fields^{44,145}. We investigated the influence of optical singularities on the spin-momentum properties of paraxial optical beams. For the HG beam without optical singularities, skyrmion-like spin textures may arise from the T-spins when the beam elliptically polarized. Then, for a LG beam with a phase singularity, the OAM property of the phase singularity results in a Berry curvature term in the T-spin, and thus a skyrmion-like spin texture arises from the T-spins when the total angular momentum of the beam is nonzero. Moreover, for the BG mode with a polarization singularity, no skyrmion-like spin texture is formed. Nevertheless, we discovered a SAM component, the direction of which is not determined by the kinetic momentum but rather the polarization

topological charge of vector vortex beam. This SAM component is a \mathbb{Z}_4 topological invariant and should be considered as an extraordinary L-spin, although its vector is perpendicular to the canonical momentum/wavevector. The findings present a field theory to describe the spin–momentum properties of paraxial systems having potential in formalizing a spin-based theory to understand wave–matter interactions in classical wave fields and motivating the exploration of novel applications in chiral manipulation and interdisciplinary research^{146–151}.

References:

1. Fert, A. Nobel Lecture: Origin, development, and future of spintronics. *Rev. Mod. Phys.* **2004**, *80*, 1517–1530. DOI: 10.1103/RevModPhys.80.1517
2. Žutić, I.; Fabian, J.; and Das Sarma, S. Spintronics: Fundamentals and applications. *Rev. Mod. Phys.* **2004**, *76*, 323–410. DOI: 10.1103/RevModPhys.76.323
3. Beth, Richard A. Mechanical detection and measurement of the angular momentum of light. *Phys. Rev.* **1936**, *50*, 115–125. DOI: 10.1103/PhysRev.50.115
4. Long, Y.; Ren, J.; and Chen, H. Intrinsic spin of elastic waves. *Proc. Natl. Acad. Sci. USA.* **2018**, *115*(40), 9951–9955. DOI: 10.1073/pnas.1808534115
5. Yuan, W.; Yang, C.; Zhang, D.; Long, Y.; Pan, Y.; Zhong, Z.; Chen, H.; Zhao, J.; and Ren, J. Observation of elastic spin with chiral meta-sources. *Nat. Commun.* **2021**, *12*, 6954:1–9. DOI: 10.1038/s41467-021-27254-z
6. Khosravi, F.; Sonner, M. M.; and Jacob, Z. Ultrafast electron cycloids driven by the transverse spin of a surface acoustic wave. *Sci. Adv.* **2021**, *7*(31), eabf7414:1–7. DOI: 10.1126/sciadv.abf7414
7. Bliokh, K. Y.; and Nori, F. Spin and orbital angular momenta of acoustic beams. *Phys. Rev. B* **2019**, *99*, 174310:1–9. DOI: 10.1103/PhysRevB.99.174310
8. Toftul, I. D.; Bliokh, K. Y.; Petrov, M. I.; and Nori, F. Acoustic radiation force and torque on small particles as measures of the canonical momentum and spin densities. *Phys. Rev. Lett.* **2019**, *123*, 183901:1–7. DOI: 10.1103/PhysRevLett.123.183901
9. Wang, S.; Zhang, G.; Wang, X.; Tong, Q.; Li, Jensen; and Ma, G. Spin-orbit interactions of transverse sound. *Nat. Commun.* **2021**, *12*, 6125:1–9. DOI: 10.1038/s41467-021-26375-9
10. Gorce, J.-B.; Bliokh, K. Y.; Xia, H.; Francois, N.; Punzmann, H.; and Shats, M. Rolling spinners on the water surface. *Sci. Adv.* **2021**, *7*, eabd4632:1–5. DOI: 10.1126/sciadv.abd46
11. Bliokh, K. Y.; Punzmann, H.; Xia, H.; Nori, F.; and Shats, M. Field theory spin and momentum in water waves. *Sci. Adv.* **2022**, *8*(3), abm1295:1–7. DOI: 10.1126/sciadv.abm1295
12. Longuet-Higgins, M. S. Spin and angular momentum in gravity waves. *Journal of Fluid Mechanics* **1980**, *97*(1), 1–25. DOI: 10.1017/S0022112080002406
13. Golat, S.; Lim, E. A.; and Rodríguez-Fortuño, F. J. Evanescent gravitational waves. *Phys. Rev. D* **2020**, *101*, 084046:1–13. DOI: 10.1103/PhysRevD.101.084046
14. Xin, S.; Long, Y.; and Ren, J. Spin angular momentum of gravitational wave interference. *New J. Phys.* **2021**, *23*, 043035:1–13. DOI: 10.1088/1367-2630/abf23f
15. Bliokh, K. Y.; Rodríguez-Fortuño, F. J.; Nori, F.; and A. V. Zayats, Spin–orbit interactions of light. *Nat. Photon.* **2015**, *9*(12), 796–808. DOI: 10.1038/NPHOTON.2015.201
16. Shi, P.; Yang, A.; Meng, F.; Chen, J.; Zhang, Y.; Xie, Z.; Du, L.; and Yuan, X. Optical near-field measurement for spin-orbit interaction of light. *Progress in Quantum Electronics* **2021**, *78*, 100341:1–20. DOI: 10.1016/j.pquantelec.2021.100341
17. Shi, P.; Du, L.; and Yuan, X. Spin photonics: from transverse spin to photonic skyrmions, *Nanophotonics* **2021**, *10*(16), 3927–3943. DOI: 10.1515/nanoph-2021-0046
18. Ling, X.; Zhou, X.; Huang, K.; Liu, Y.; Qiu, C.-W.; Luo, H.; and Wen, S. Recent advances in the spin Hall effect of light.

Rep. Prog. Phys. **2017**, *80*, 066401:1-17. DOI: 10.1088/1361-6633/aa5397

19. Onoda, M.; Murakami, S.; and Nagaosa, N. Hall effect of light. *Phys. Rev. Lett.* **2004**, *93*, 083901:1-4. DOI: 10.1103/PhysRevLett.93.083901
20. Hosten, O.; and Kwiat, P. Observation of the spin Hall effect of light via weak measurements. *Science* **2008**, *319*, 787-790. DOI: 10.1126/science.1152697
21. Kavokin, A.; Malpuech, G.; and Glazov, M. Optical spin Hall effect. *Phys. Rev. Lett.* **2005**, *95*, 136601:1-4. DOI: 10.1103/PhysRevLett.95.136601
22. Zhu, W.; Zheng, H.; Zhong, Y.; Yu, J.; and Chen, Z. Wave-vector-varying Pancharatnam-Berry phase photonic spin Hall effect. *Phys. Rev. Lett.* **2021**, *126*, 083901:1-6. DOI: 10.1103/PhysRevLett.126.083901
23. Bardon-brun, T.; Delande, D.; and Cherroret, N. Spin Hall effect of light in a random medium. *Phys. Rev. Lett.* **2019**, *123*, 043901:1-5. DOI: 10.1103/PhysRevLett.123.043901
24. Fu, S.; Guo, C.; Liu, G.; Li, Y.; Yin, H.; Li, Z.; and Chen, Z. Spin-orbit optical Hall effect. *Phys. Rev. Lett.* **2019**, *123*, 243904:1-6. DOI: 10.1103/PhysRevLett.123.243904
25. Ling, X.; Guan, F.; Cai, X.; Ma, S.; Xu, H.; He, Q.; Xiao, S.; and Zhou, L. Topology-induced phase transitions in spin-orbit photonics. *Laser Photon. Rev.* **2021**, *15*, 2000492:1-10. DOI: 10.1002/lpor.202000492
26. Kim, M.; Lee, D.; Cho, H.; Min, B.; and Rho, J. Spin Hall effect of light with near-unity efficiency in the microwave. *Laser Photonics Rev.* **2021**, *15*, 2000393:1-7. DOI: 10.1002/lpor.202000393
27. Marrucci, L.; Manzo, C.; and Paparo, D. Optical spin-to-orbital angular momentum conversion in inhomogeneous anisotropic media. *Phys. Rev. Lett.* **2006**, *96*, 163905:1-4. DOI: 10.1103/PhysRevLett.96.163905
28. Zhao, Y.; Edgar, J. Scott; Jeffries, Gavin D. M.; McGloin, D.; and Chiu, Daniel T. Spin-to-orbital angular momentum conversion in a strongly focused optical beam. *Phys. Rev. Lett.* **2007**, *99*, 073901:1-4. DOI: 10.1103/PhysRevLett.99.073901
29. Vuong, L. T.; Adam, A. J. L.; Brok, J. M.; Planken, P. C. M.; and Urbach, H. P. Electromagnetic spin-orbit interactions via scattering of subwavelength apertures. *Phys. Rev. Lett.* **2010**, *104*, 083903:1-4. DOI: 10.1103/PhysRevLett.104.083903
30. Haldane, F. D. M.; and Raghu, S. Possible realization of directional optical waveguides in photonic crystals with broken time-reversal symmetry. *Phys. Rev. Lett.* **2008**, *100*, 013904:1-4. DOI: 10.1103/PhysRevLett.100.013904
31. Wang, Z.; Chong, Y. D.; Joannopoulos, J. D.; and Soljačić, M. Reflection-free one-way edge modes in a gyromagnetic photonic crystal. *Phys. Rev. Lett.* **2008**, *100*, 013905:1-4. DOI: 10.1103/PhysRevLett.100.013905
32. Ozawa, T.; Price, H. M.; Amo, A.; Goldman, N.; Hafezi, M.; Lu, L.; Rechtsman, M. C.; Schuster, D.; Simon, J.; Zilberberg, O.; and Carusotto, I. Topological photonics. *Rev. Mod. Phys.* **2019**, *91*, 015006:1-76. DOI: 10.1103/RevModPhys.91.015006
33. Bliokh, K. Y.; and Nori, F. Transverse and longitudinal angular momenta of light. *Phys. Rep.* **2015**, *592*, 1. DOI: 10.1016/j.physrep.2015.06.003
34. Aiello, A.; Banzer, P.; Neugebauer, M.; and Leuchs, G. From transverse angular momentum to photonic wheels. *Nat. Photon.* **2015**, *9*(12), 789-795. DOI: 10.1038/nphoton.2015.203
35. Bliokh, K. Y.; Bekshaev, A. Y.; and Nori, F.; Extraordinary momentum and spin in evanescent waves. *Nat. Commun.* **2014**, *5*, 3300:1-8. DOI: 10.1038/ncomms4300 (2014).
36. Bliokh, K. Y.; Smirnova, D.; and Nori, F. Quantum spin Hall effect of light. *Science* **2015**, *348*, 1448-1451. DOI: 10.1126/science.aaa9519
37. Antognozzi, M.; Bermingham, C. R.; Harniman, R. L.; Simpson, S.; Senior, J.; Hayward, R.; Hoerber, H.; Dennis, M. R.; Bekshaev, A. Y.; Bliokh, K. Y.; and Nori, F. Direct measurements of the extraordinary optical momentum and transverse spin-dependent force using a nano-cantilever. *Nat. Phys.* **2016**, *12*, 731-735. DOI: 10.1038/nphys3732
38. Bliokh, K. Y.; Rodríguez-Fortuño, F. J.; Bekshaev, A. Y.; Kivshar, Y. S.; and Nori, F. Electric-current-induced unidirectional propagation of surface plasmon-polaritons. *Opt. Lett.* **2018**, *43*, 963-966. DOI: 10.1364/OL.43.000963
39. Bekshaev, A. Y. Transverse spin and the hidden vorticity of propagating light fields. *Journal of the Optical Society of America A* **2022**, *39*(9), 1577-1583. DOI: 10.1364/JOSAA.466360

40. Bekshaev, A. Y.; Angelsky, O. V.; Zheng, J.; Hanson, S. G.; and Zenkova, C. Yu. Microscopic analysis of the energy, momentum, and spin distributions in a surface plasmon-polariton wave. *Optical Materials Express* **2021**, *11*(7), 2165-2191. DOI: 10.1364/OME.428201
41. Shi, P.; Du, L.-P.; Li, C.-C.; Zayats, A.; and Yuan, X.-C. Transverse spin dynamics in structured electromagnetic guided waves. *Proc. Natl. Acad. Sci. USA* **2021**, *118*(6), e2018816118:1-5. DOI: 10.1073/pnas.2018816118
42. Shi, P.; Lei, X.; Zhang, Q.; Li, H.; Du, L.; and Yuan, X. Intrinsic spin-momentum dynamics of surface electromagnetic waves in dispersive interfaces. *Phys. Rev. Lett.* **2022**, *128*, 218904:1-6. DOI: 10.1103/PhysRevLett.128.213904
43. Bliokh, K. Y.; and Nori, F. Transverse spin of a surface polariton. *Phys. Rev. A* **2012**, *85*(6), 061801(R):1-5. DOI: 10.1103/PhysRevA.85.061801
44. Peng, L.; Duan, L.; Wang, K.; Gao, F.; Zhang, L.; Wang, G.; Yang, Y.; Chen, H.; and Zhang, S. Transverse photon spin of bulk electromagnetic waves in bianisotropic media. *Nat. Photon.* **2019**, *13*, 878-882. DOI: 10.1038/s41566-019-0521-4
45. Picardi, M. F.; Bliokh, K. Y.; Rodríguez-Fortuño, F. J.; Alpegiani, F.; and Nori, F. Angular momenta, helicity, and other properties of dielectric-fiber and metallic-wire modes. *Optica* **2018**, *5*, 1016-1026. DOI: 10.1364/OPTICA.5.001016
46. Neugebauer, M.; Bauer, T.; Aiello, A.; and Banzer, P. Measuring the transverse spin density of light. *Phys. Rev. Lett.* **2015**, *114*, 063901:1-5. DOI: 10.1103/PhysRevLett.114.063901
47. Neugebauer, M.; Eismann, Jörg S.; Bauer, T.; and Banzer, P. Magnetic and electric transverse spin density of spatially confined light. *Phys. Rev. X* **2018**, *8*, 021042:1-8. DOI: 10.1103/PhysRevX.8.021042
48. Eismann, J. S.; Banzer, P.; and Neugebauer, M. Spin-orbit coupling affecting the evolution of transverse spin. *Phys. Rev. Research* **2019**, *1*, 033143:1-4. DOI: 10.1103/PhysRevResearch.1.033143
49. Shi, P.; Du, L.; and Yuan, X.-C. Structured spin angular momentum in highly focused cylindrical vector vortex beams for optical manipulation. *Opt. Express* **2018**, *26*(8), 23449-23459. DOI: 10.1364/OE.26.023449
50. Shi, P.; Du, L.; and Yuan, X.-C. Optical manipulation with electric and magnetic transverse spin through multilayered focused configuration. *Appl. Phys. Express* **2019**, *12*, 032001:1-5. DOI: 10.7567/1882-0786/aafca1
51. Bekshaev, A.Y.; Bliokh, K. Y.; and Nori, F. Transverse spin and momentum in two-wave interference. *Phys. Rev. X* **2015**, *5*, 011039:1-9. DOI: 10.1103/PhysRevX.5.011039
52. Aiello, A.; and Banzer, P. The ubiquitous photonic wheel. *J. Opt.* **2016**, *18*, 085605:1-8. DOI: 10.1088/2040-8978/18/8/085605
53. Eismann, J. S.; Nicholls, L. H.; Roth, D. J.; Alonso, M. A.; Banzer, P.; Rodríguez-Fortuño, F. J.; Zayats, A. V.; Nori, F.; and Bliokh, K. Y. Transverse spinning of unpolarized light. *Nat. Photon.* **2020**, *15*, 156-161. DOI: 10.1038/s41566-020-00733-3
54. Chen, Y.; Wang, F.; Dong, Z.; Cai, Y.; Norrman, A.; Gil, J. J.; Friberg, A. T.; and Setälä, T. Structure of transverse spin in focused random light. *Phys. Rev. A* **2021**, *104*, 013516:1-8. DOI: 10.1103/PhysRevA.104.013516
55. Chen, Y.; Norrman, A.; Ponomarenko, S. A.; and Friberg, A. T. Spin density in partially coherent surface-plasmon-polariton vortex fields. *Phys. Rev. A* **2021**, *103*, 063511:1-7. DOI: 10.1103/PhysRevA.103.063511
56. Chen, Y.; Norrman, A.; Ponomarenko, S. A.; and Friberg, A. T. Partially coherent surface plasmon polariton vortex fields. *Phys. Rev. A* **2019**, *100*, 053833:1-14. DOI: 10.1103/PhysRevA.100.053833d
57. Shi, P.; Yang, A.; Yin, X.; Du, L.; Lei, X., and Yuan, X., Spin decomposition and topological properties in a generic electromagnetic field. 2022-11-12. *arXiv*:2108.00725v4. URL: <https://doi.org/10.48550/arXiv.2108.00725>
58. Mechelan, T. Van; and Jacob, Z. Universal spin-momentum locking of evanescent waves. *Optica* **2016**, *3*(2), 118-126. DOI: 10.1364/OPTICA.3.000118
59. Rodríguez-Fortuño, F. J.; Marino, G.; Ginzburg, P.; O'Connor, D.; Martínez, A.; Wurtz, G. A.; Zayats, A. V. Near-field interference for the unidirectional excitation of electromagnetic guided modes. *Science* **2013**, *340*, 328-330. DOI: 10.1126/science.1233739
60. Lin, J.; Mueller, J. P. Balthasar; Wang, Q.; Yuan, G.; Antoniou, N.; Yuan, X.-C.; and Capasso, F. Polarization-controlled tunable directional coupling of surface plasmon polaritons. *Science* **2013**, *340*(6130), 331-334. DOI:

10.1126/science.1233746

61. Petersen, J.; Volz, J.; and Rauschenbeutel, A. Chiral nanophotonic waveguide interface based on spin-orbit interaction of light. *Science* **2014**, *346*(6205), 67-71. DOI: 10.1126/science.1257671
62. O'Connor, D.; Ginzburg, P.; Rodríguez-Fortuño, F. J.; Wurtz, G. A.; and Zayats, A. V. Spin-orbit coupling in surface plasmon scattering by nanostructures. *Nat. Commun.* **2014**, *5*(1), 53271:1-7. DOI: 10.1038/ncomms6327 (2014).
63. Rodríguez-Fortuño, F. J.; Barber-Sanz, I.; Puerto, D.; Griol, A.; and Martinez, A. Resolving light handedness with an on-chip silicon microdisk. *ACS Photonics* **2014**, *1*(9), 762-767. DOI: 10.1021/ph500084b
64. Söllner, I.; Mahmoodian, S.; Hansen, S. L.; Midolo, L.; Javadi, A.; Kiršanskė, G.; Pregnolato, T.; El-Ella, H.; Lee, E.-H.; Song, J.-D.; Stobbe, S.; and Lodahl, P. Deterministic photon-emitter coupling in chiral photonic circuits. *Nat. Nanotech.* **2015**, *10*, 775-778. DOI: 10.1038/NNANO.2015.159
65. Feber, B. le; Rotenberg, N.; and Kuipers, L. Nanophotonic control of circular dipole emission. *Nat. Commun.* **2015**, *6*, 6695:1-6. DOI: 10.1038/ncomms7695
66. Yang, A.-P.; Du, L.-P.; Meng, F.-F.; and Yuan, X.-C. Optical transverse spin coupling through a plasmonic nanoparticle for particle-identification and field-mapping. *Nanoscale* **2018**, *10*, 9286-9290. DOI: 10.1039/c8nr01618f
67. Guo, Z.; Long, Y.; Jiang, H.; Ren, J.; and Chen, H. Anomalous unidirectional excitation of high-k hyperbolic modes using allelectric metasources. *Adv. Photon.* **2021**, *3*, 036001:1-10. DOI: 10.1117/1.AP.3.3.036001
68. Du, L. P.; Yang, A. P.; Zayats, A. V.; and Yuan, X. C. Deep-subwavelength features of photonic skyrmions in a confined electromagnetic field with orbital angular momentum. *Nat. Phys.* **2019**, *15*, 650-654. DOI: 10.1038/s41567-019-0487-7
69. Y. Dai, Z. Zhou, A. Ghosh, R. S. K. Mong, A. Kubo, C.-B. Huang, and H. Petek, Plasmonic topological quasiparticle on the nanometre and femtosecond scales, *Nature* **2020**, *588*, 616-619. DOI: 10.1038/s41586-020-3030-1
70. Tsesses, S.; Cohen, K.; Ostrovsky, E.; Gjonaj, B.; and Bartal, G. Spin-orbit interaction of light in plasmonic lattices. *Nano Lett.* **2019**, *19*(6), 4010-4016. DOI: 10.1021/acs.nanolett.9b01343
71. Shi, P.; Du, L.; and Yuan, X.-C. Strong spin-orbit interaction of photonic skyrmions at the general optical interface. *Nanophotonics* **2020**, *9*(15), 4619-4628. DOI: 10.1515/nanoph-2020-0430
72. Li, C. C.; Shi, P.; Du, L. P.; and Yuan, X.-C. Mapping the near-field spin angular momenta in the structured surface plasmon polariton field. *Nanoscale* **2020**, *12*, 13674-13679. DOI: 10.1039/d0nr00618a
73. Lei, X.; Yang, A.; Shi, P.; Xie, Z.; Du, L.; Zayats, Anatoly V.; and Yuan, X. Photonic spin lattices: symmetry constraints for skyrmion and meron topologies. *Phys. Rev. Lett.* **2021**, *127*, 237403:1-6. DOI: 10.1103/PhysRevLett.127.237403
74. Ghosh, A.; Yang, S.; Dai, Y.; Zhou, Z.; Wang, T.; Huang, C.; and Petek, H. A topological lattice of plasmonic merons. *Applied Physics Reviews* **2021**, *8*, 041413:1-10. DOI: 10.1063/5.0062133
75. Shi, P.; Du, L.; Li, M.; and Yuan, X.-C. Symmetry-Protected Photonic Chiral Spin Textures by Spin–Orbit Coupling. *Laser & Photonics Review* **2021**, *15*, 202000554:1-9. DOI: 10.1002/lpor.202000554
76. Zhang, Q.; Xie, Z.; Du, L.; Shi, P.; and Yuan, X. Bloch-type photonic skyrmions in optical chiral multilayers. *Phys. Rev. Research* **2021**, *3*, 023109:1-10. DOI: 10.1103/PhysRevResearch.3.023109
77. Dai, Y.; Zhou, Z.; Ghosh, A.; Kapoor, K.; Dąbrowski, M.; Kubo, A.; Huang, C.-B.; and Petek, H. Ultrafast microscopy of a twisted plasmonic spin skyrmion. *Applied Physics Reviews* **2022**, *9*, 011420:1-9. DOI: 10.1063/5.0084482
78. Zhang, Q.; Xie, Z.; Shi, P.; Yang, H.; He, H.; Du, L.; and Yuan, X. Optical topological lattices of Bloch-type skyrmion and meron topologies. *Photonics Research* **2022**, *10*(4), 947-957. DOI: 10.1364/PRJ.447311
79. Wang, S. B.; and Chan, C. T. Lateral optical force on chiral particles near a surface. *Nat. Commun.* **2014**, *5*, 3307:1-8. DOI: 10.1038/ncomms4307
80. Hayat, A.; Mueller, J. P. B.; and Capasso, F. Lateral chirality-sorting optical forces. *Proc. Natl Acad. Sci. USA* **2015**, *112*, 13190-13194. DOI: 10.1073/pnas.1516704112
81. Araneda, G.; Walser, S.; Colombe, Y.; Higginbottom, D. B.; Volz, J.; Blatt, R.; and Rauschenbeutel, A. Wavelength-scale errors in optical localization due to spin-orbit coupling of light. *Nat. Phys.* **2019**, *15*, 17-21. DOI: 10.1038/s41567-018-0301-

y

82. Zhu, T.; Lou, Y.; Zhou, Y.; Zhang, J.; Huang, J.; Li, Y.; Luo, H.; Wen, S.; Zhu, S.; Gong, Q.; Qiu, M.; and Ruan, Z. Generalized spatial differentiation from the spin Hall effect of light and its application in image processing of edge detection. *Phys. Rev. Applied* **2019**, *11*, 034043:1-13. DOI: 10.1103/PhysRevApplied.11.034043
83. Zhou, J.; Qian, H.; Chen, C.-F.; Zhao, J.; Li, G.; Wu, Q.; Luo, H.; Wen, S.; and Liu, Z. Optical edge detection based on high-efficiency dielectric metasurface. *Proc. Natl. Acad. Sci. USA.* **2019**, *116*(23), 11137-11140. DOI: 10.1073/pnas.1820636116
84. Zhou, J.; Liu, S.; Qian, H.; Li, Y.; Luo, H.; Wen, S.; Zhou, Z.; Guo, G.; Shi, B.; and Liu, Z. Metasurface enabled quantum edge detection. *Sci. Adv.* **2020**, *6*(51), eabc4385:1-7. DOI: 10.1126/sciadv.abc4385
85. Xu, D.; He, S.; Zhou, J.; Chen, S.; Wen, S.; and Luo, H. Optical analog computing of two-dimensional spatial differentiation based on the Brewster effect. *Optics Letters* **2020**, *45*(24), 6867-6870. DOI: 10.1364/OL.413104
86. He, S.; Zhou, J.; Chen, S.; Shu, W.; Luo, H.; and Wen, S. Wavelength-independent optical fully differential operation based on the spin-orbit interaction of light. *APL Photonics* **2020**, *5*, 036105:1-6. DOI: 10.1063/1.5144953
87. Xu, D.; He, S.; Zhou, J.; Chen, S.; Wen, S.; and Luo, H. Goos-Hänchen effect enabled optical differential operation and image edge detection. *Appl. Phys. Lett.* **2020**, *116*, 211103:1-5. DOI: 10.1063/5.0006483
88. He, S.; Zhou, J.; Chen, S.; Shu, W.; Luo, H.; and Wen, S. Spatial differential operation and edge detection based on the geometric spin Hall effect of light. *Optics Letters* **2020**, *45*(4), 877-880. DOI: 10.1364/OL.386224
89. Zhou, J.; Qian, H.; Zhao, J.; Tang, M.; Wu, Q.; Lei, M.; Luo, H.; Wen, S.; Chen, S.; and Liu, Z. Two-dimensional optical spatial differentiation and high-contrast imaging. *National Science Review* **2021**, *8*(6), nwaa176:1-8. DOI: 10.1093/nsr/nwaa176
90. Wang, R.; He, S.; Chen, S.; Shu, W.; Wen, S.; and Luo, H. Computing metasurfaces enabled chiral edge image sensing. *iScience* **2022**, *25*(7), 104532:1-14. DOI: 10.1016/j.isci.2022.104532
91. Xiao, T.; Yang, H.; Yang, Q.; Xu, D.; Wang, R.; Chen, S.; and Luo, H. Realization of tunable edge-enhanced images based on computing metasurfaces. *Optics Letters* **2022**, *47*(4), 925-928. DOI: 10.1364/OL.450988
92. Liu, J.; Yang, Q.; Chen, S.; Xiao, Z.; Wen, S.; and Luo, H. Intrinsic Optical Spatial Differentiation Enabled Quantum Dark-Field Microscopy. *Phys. Rev. Lett.* **2022**, *128*, 193601:1-6. DOI: 10.1103/PhysRevLett.128.193601
93. Y. Wang, Q. Yang, S. He, R. Wang, and H. Luo, Computing metasurfaces enabled broad-band vectorial differential interference contrast microscopy. *ACS Photonics.* **2022**. DOI: 10.1021/acspophotonics.2c00882
94. Zhou, X.; Ling, X.; Luo, H.; and Wen, S. Identifying graphene layers via spin Hall effect of light. *Appl. Phys. Lett.* **2012**, *101*, 251602:1-4. DOI: 10.1063/1.4772502
95. Chen, S.; Ling, X.; Shu, W.; Luo, H.; and Wen, S. Precision measurement of the optical conductivity of atomically thin crystals via photonic spin Hall effect. *Phys. Rev. Applied* **2020**, *13*, 014057:1-10. DOI: 10.1103/PhysRevApplied.13.014057
96. Lei, X.; Du, L.; Yuan, X.; and Zayats, Anatoly V. Optical spin-orbit coupling in the presence of magnetization: photonic skyrmion interaction with magnetic domains. *Nanophotonics* **2021**, *10*(14), 3667-3675. DOI: 10.1515/nanoph-2021-0201
97. Neugebauer, M.; Wozniak, P.; Bag, A.; Leuchs, G.; and Banzer, P. Polarization-controlled directional scattering for nanoscopic position sensing. *Nat. Commun.* **2016**, *7*, 11286:1-5. DOI: 10.1038/ncomms11286
98. Du, L.; Yang, A.; and Yuan, X. Ultrasensitive displacement sensing method and device based on local spin characteristics. *US Patent App.* **2021**, *16/303,773*.
99. Lodahl, P.; Mahmoodian, S.; Stobbe, S.; Rauschenbeutel, A.; Schneeweiss, P.; Volz, J.; Pichler, H.; and Zoller, P. Chiral quantum optics. *Nature* **2017**, *541*, 473-480. DOI: 10.1038/nature21037
100. Forbes, A.; Oliveira, Michael de; and Dennis, Mark R. Structured light. *Nat. Photon.* **2021**, *15*, 253-261. DOI: 10.1038/s41566-021-00780-4
101. He, C.; Shen, Y.; and Forbes, A. Towards higher-dimensional structured light. *Light: Science & Applications* **2022**, *11*, 205:1-17. DOI: 10.1038/s41377-022-00897-3
102. Chen, J.; Wan, C.; and Zhan, Q. Engineering photonic angular momentum with structured light: a review. *Adv. Photon.*

2021, 3(6), 064001:1-15. DOI: 10.1117/1.AP.3.6.064001

103. Angelsky, O. V.; Bekshaev, A. Y.; Hanson, S. G.; Zenkova, C. Yu; Mokhun, I. I.; and Jun, Z. Structured light: ideas and concepts. *Front. Phys.* **2020**, *8*, 114:1-26. DOI: 10.3389/fphy.2020.00114
104. Shen, Y.; Wang, X.; Xie, Z.; Min, C.; Fu, X.; Liu, Q.; Gong, M.; and Yuan, X. Optical vortices 30 years on: OAM manipulation from topological charge to multiple singularities. *Light: Science & Applications* **2019**, *8*, 90:1-29. DOI: 10.1038/s41377-019-0194-2
105. Zhan, Q. Cylindrical vector beams: from mathematical concepts to applications. *Advances in Optics and Photonics* **2009**, *1*(1), 1-57. DOI: 10.1364/AOP.1.000001
106. Zdagkas, A.; McDonnell, C.; Deng, J.; Shen, Y.; Li, G.; Ellenbogen, T.; Papasimakis, N.; and Zheludev, N. I. Observation of toroidal pulses of light. *Nat. Photon.* **2022**, *16*, 523-528. DOI: 10.1038/s41566-022-01028-5
107. Gao, S.; Speirits, F. C.; Castellucci, F.; Franke-Arnold, S.; and Barnett, S. M. Paraxial skyrmionic beams. *Phys. Rev. A* **2020**, *102*, 053513:1-6. DOI: 10.1103/PhysRevA.102.053513
108. Shen, Y.; Hou, Y.; Papasimakis, N.; and Zheludev, N. I. Supertoroidal light pulses as electromagnetic skyrmions propagating in free space. *Nat. Commun.* **2021**, *12*, 5891:1-9. DOI: 10.1038/s41467-021-26037-w
109. Sugic, D.; Droop, R.; Otte, E.; Ehrmanntraut, D.; Nori, F.; Ruostekoski, J.; Denz, C.; and Dennis, Mark R. Particle-like topologies in light. *Nat. Commun.* **2021**, *12*, 6785:1-10. DOI: 10.1038/s41467-021-26171-5
110. Shen, Y. Topological bimeronic beams. *Optics Letters* **2021**, *46*(15), 3737-3740. DOI: 10.1364/OL.431122
111. Lin, W.; Ota, Y.; Arakawa, Y.; and Iwamoto, S. Microcavity-based generation of full Poincaré beams with arbitrary skyrmion numbers. *Phys. Rev. Research* **2021**, *3*, 023055:1-12. DOI: 10.1103/PhysRevResearch.3.023055
112. Deng, Z.; Shi, T.; Krasnok, A.; Li, X.; and Alù, A. Observation of localized magnetic plasmon skyrmions. *Nat. Commun.* **2022**, *13*, 8:1-7. DOI: 10.1038/s41467-021-27710-w
113. Shen, Y.; Martínez, E. C.; and Rosales-Guzmán, C. Generation of optical Skyrmions with tunable topological textures. *ACS Photonics* **2022**, *9*(1), 296-303. DOI: 10.1021/acsphotonics.1c01703
114. Parmee, C. D.; Dennis, M. R.; and Ruostekoski, J. Optical excitations of Skyrmions, knotted solitons, and defects in atoms. *Communications Physics* **2022**, *5*, 54:1-8. DOI: 10.1038/s42005-022-00829-y
115. Yang, J.; Zheng, X.; Wang, J.; Pan, Y.; Zhang, A.; Cui, T.-J.; Vandebosch, Guy A. E. Symmetry-Protected Spoof Localized Surface Plasmonic Skyrmion. *Laser & Photonics Reviews* **2022**, *16*(6), 202200007:1-7. DOI: 10.1002/lpor.202200007
116. Zhu, J., Liu, S., and Zhang, Y.-S., Synthesis and observation of optical skyrmionic structure in free space. 2021-03-25. *arXiv:2103.11293*. URL: <https://doi.org/10.48550/arXiv.2103.11293>
117. Shen, Y., Zhang, Q., Shi, P., Du, L., Zayats, A. V., and Yuan, X., Topological quasiparticles of light: Optical skyrmions and beyond. 2022-05-20. *arXiv:2205.10329*. URL: <https://doi.org/10.48550/arXiv.2205.10329>
118. McWilliam, A., Cisowski, C. M., Ye, Z., Speirits, F. C., Götte, J. B., Barnett, S. M., Franke-Arnold, S., Topological approach of characterizing optical Skyrmions and Skyrmion lattices. 2022-09-14. *arXiv:2209.06734*. URL: <https://doi.org/10.48550/arXiv.2209.06734>
119. Berry, M. V. Optical currents. *J. Opt. Pure Appl. Opt.* **2009**, *11*(9), 094001:1-12. DOI: 10.1088/1464-4258/11/9/094001
120. Berry, M. V.; and Shukla, P. Geometry of 3D monochromatic light: local wavevectors, phases, curl forces, and superoscillations. *J. Opt.* **2019**, *21*, 064002:1-13. DOI: 10.1088/2040-8986/ab14c4
121. Bekshaev, A.; Bliokh, K. Y.; and Soskin, M. Internal flows and energy circulation in light beams. *J. Opt.* **2011**, *13*, 053001:1-32. DOI: 10.1088/2040-8978/13/5/053001
122. Pfeifer, Robert N. C.; Nieminen, T. A.; Heckenberg, N. R.; and Rubinsztein-Dunlop, H. Colloquium: Momentum of an electromagnetic wave in dielectric media. *Rev. Mod. Phys.* **2007**, *79*, 1197-1216. DOI: 10.1103/RevModPhys.79.1197
123. Bliokh, K. Y.; Bekshaev, Aleksandr Y.; and Nori, F. Optical momentum and angular momentum in complex media: from the Abraham–Minkowski debate to unusual properties of surface plasmon polaritons. *New J. Phys.* **2017**, *19*, 123014:1-23.

DOI: 10.1088/1367-2630/aa8913

124. Kane, C. L.; and Mele, E. J. Z2 topological order and the quantum spin Hall effect. *Phys. Rev. Lett.* **95**, 146802:1-4 (2005). DOI: 10.1103/PhysRevLett.95.146802
125. J. J. Sakurai, *Modern quantum mechanics*, Addison-Wesley, San Francisco, CA, 1994.
126. Milione, G.; Sztul, H. I.; Nolan, D. A.; and Alfano, R. R. Higher-Order Poincaré Sphere, Stokes Parameters, and the Angular Momentum of Light. *Phys. Rev. Lett.* **2011**, *107*, 053601:1-4. DOI: 10.1103/PhysRevLett.107.053601
127. Milione, G.; Evans, S.; Nolan, D. A.; and Alfano, R. R. Higher order Pancharatnam-Berry phase and the angular momentum of light. *Phys. Rev. Lett.* **2012**, *108*, 190401. DOI: 10.1103/PhysRevLett.108.190401
128. Liu, Y.; Ling, X.; Yi, X.; Zhou, X.; Luo, H.; and We, S. Realization of polarization evolution on higher-order Poincare sphere with metasurface. *Appl. Phys. Lett.* **2014**, *104*, 191110:1-4. DOI: 10.1063/1.4878409
129. Chen, S.; Zhou, X.; Liu, Y.; Ling, X.; Luo, H.; and Wen, S. Generation of arbitrary cylindrical vector beams on the higher order Poincaré sphere. *Optics Letters* **2014**, *39*(18), 5274:1-4. DOI: 10.1364/OL.39.005274
130. Ren, Z.; Kong, L.; Li, S.; Qian, S.; Li, Y.; Tu, C.; and Wang, H.-T. Generalized Poincaré sphere. *Optics Express* **2015**, *23*(20), 26586-26595. DOI: 10.1364/OE.23.026586
131. Barnett, S. M. Optical Dirac equation. *New J. Phys.* **2014**, *16*, 093008:1-25. DOI: 10.1088/1367-2630/16/9/093008
132. Bialynicki-Birula, I.; and Bialynicka-Birula, Z. The role of the Riemann–Silberstein vector in classical and quantum theories of electromagnetism. *J. Phys. Math. Theor.* **2013**, *46*, 053001:1-32. DOI: 10.1088/1751-8113/46/5/053001
133. Tomita, A.; and Chiao, R. Y. Observation of Berry's topological phase by use of an optical fiber. *Phys. Rev. Lett.* **1986**, *57*, 937; *Erratum Phys. Rev. Lett.* **1986**, *57*, 2471. DOI: 10.1103/PhysRevLett.57.937
134. Bliokh, K. Y.; Niv, A.; Kleiner, V.; and Hasman, E. Geometrodynamics of spinning light. *Nat. Photon.* **2008**, *2*, 748-753. DOI: 10.1038/nphoton.2008.229
135. Bliokh, K. Y. Geometrodynamics of polarized light: Berry phase and spin Hall effect in a gradient-index medium. *J. Opt. Pure Appl. Opt.* **2009**, *11*, 094009:1-14. DOI: 10.1088/1464-4258/11/9/094009
136. Wolf, E. A scalar representation of electromagnetic fields: II. *Proc. Phys. Soc.* **1959**, *74*, 269-280. DOI: 10.1088/0370-1328/74/3/305
137. Berry, M. V. Quantal phase factors accompanying adiabatic changes. *Proc. R. Soc. A* **1984**, *392*, 45-57. DOI: 10.1098/rspa.1984.0023
138. Bliokh, K. Y.; Alonso, M. A.; Ostrovskaya, E. A.; and Aiello, A. Angular momenta and spin-orbit interaction of nonparaxial light in free space. *Phys. Rev. A* **2010**, *82*, 063825:1-7. DOI: 10.1103/PhysRevA.82.063825
139. Fernandez-Corbaton, I.; Zambrana-Puyalto, X.; Tischler, N.; Vidal, X.; Juan, M.-L.; and Molina-Terriza, G. Electromagnetic duality symmetry and helicity conservation for the macroscopic Maxwell's equations. *Phys. Rev. Lett.* **2013**, *111*, 060401:1-5. DOI: 10.1103/PhysRevLett.111.060401
140. Cameron, R. P.; and Barnett, S. M. Electric-magnetic symmetry and Noether's theorem. *New J. Phys.* **2012**, *14*, 123019:1-27. DOI: 10.1088/1367-2630/14/12/123019
141. Bliokh, K. Y.; Dressel, J.; and Nori, F. Conservation of the spin and orbital angular momenta in electromagnetism. *New J. Phys.* **2014**, *16*, 093037:1-21. DOI: 10.1088/1367-2630/16/9/093037
142. Allen, L.; Beijersbergen, M. W.; Spreeuw, R. J.; and Woerdman, J. P. Orbital angular momentum of light and the transformation of Laguerre-Gaussian laser modes. *Phys. Rev. A* **1992**, *45*(11), 8185-8189. DOI: 10.1103/PhysRevA.45.8185
143. Huang, K.; Shi, P.; Cao, G. W.; Li, K.; Zhang, X. B.; and Li, Y. P. Vector-vortex Bessel–Gauss beams and their tightly focusing properties. *Optics Letters* **2011**, *36*(6), 888-890. DOI: 10.1364/OL.36.000888
144. Joseph, Daniel D. Helmholtz decomposition coupling rotational to irrotational flow of a viscous fluid. *Proc. Natl. Acad. Sci. USA* **2006**, *103*(39), 14272-14277. DOI: 10.1073/pnas.0605792103
145. Ge, H.; Xu, X.-Y.; Liu, L.; Xu, R.; Lin, Z.-K.; Yu, S.-Y.; Bao, M.; Jiang, J.-H.; Lu, M.-H.; and Chen, Y.-F. Observation of acoustic skyrmions. *Phys. Rev. Lett.* **2021**, *127*, 144502:1-6. DOI: 10.1103/PhysRevLett.127.144502

146. Chen, Y.; Du, W.; Zhang, Q.; Ovando, O. A.; Wu, J.; Xu, Q.; Liu, N.; Okamoto, H.; Govorov, A. O.; Xiong, Q.; and Qiu, C.-W. Multidimensional nanoscopic chiroptics. *Nat. Rev. Phys.* **2022**, *4*, 113-124. DOI: 10.1038/s42254-021-00391-6
147. Hentschel, M.; Schäferling, M.; Duan, X.; Giessen, H.; and Liu, N. Chiral plasmonics. *Sci. Adv.* **2017**, *3*, e1602735:1-12. DOI: 10.1126/sciadv.1602735
148. Zhang, Y.; Min, C.; Dou, X.; Wang, X.; Urbach, H. P.; Somekh, M. G.; and Yuan, X. Plasmonic tweezers: for nanoscale optical trapping and beyond. *Light: Science & Applications* **2021**, *10*, 59:1-41. DOI: 10.1038/s41377-021-00474-0
149. Yang, Y.; Ren, Y.; Chen, M.; Arita, Y.; and Rosales-Guzmán, C. Optical trapping with structured light: a review. *Adv. Photon.* **2021**, *3*(3), 034001:1-40. DOI: 10.1117/1.AP.3.3.034001
150. Ni, J.; Liu, S.; Wu, D.; Lao, Z.; Wang, Z.; Huang, K.; Ji, S.; Li, J.; Huang, Z.; Xiong, Q.; Hu, Y.; Chu, J.; and Qiu, C.-W. Gigantic vortical differential scattering as amonochromatic probe for multiscale chiral structures. *Proc. Natl. Acad. Sci. USA* **2021**, *118*(2), e202005511:1-7. DOI: 10.1073/pnas.2020055118
151. Rauschenbeutel, A.; and Schneeweiss, P. Chiral quantum optics goes electric. *Nat. Photon.* **2022**, *16*, 261-262. DOI: 10.1038/s41566-022-00982-4